Electronic Structure Sensitivity to Hydration in Smectite Clays Unveiled by Near-Ambient Pressure X-ray Photoelectron Spectroscopy

Anthony Boucly, François Rochet, Héloïse Tissot, Quentin Arnoux, Jean-Jacques Gallet, Fabrice Bournel, Stéphane Carniato, Emmanuelle Dubois, Laurent Michot, Virginie Marry

To cite this version:

Anthony Boucly, François Rochet, Héloïse Tissot, Quentin Arnoux, Jean-Jacques Gallet, et al.. Electronic Structure Sensitivity to Hydration in Smectite Clays Unveiled by Near-Ambient Pressure X-ray Photoelectron Spectroscopy. Journal of Physical Chemistry C, 2024, 128 (40), pp.17112-17123. 10.1021/acs.jpcc.4c04072 . hal-04734886

HAL Id: hal-04734886
https://hal.science/hal-04734886v1

Submitted on 14 Oct 2024

Electronic Structure Sensitivity to Hydration in Smectite Clays Unveiled by Near Ambient Pressure X-ray Photoelectron Spectroscopy

Anthony Boucly[1]**, François Rochet*[1]**, Héloïse Tissot*[2]*, Quentin Arnoux*[1†]*, Jean-Jacques Gallet*[1,3]*, Fabrice Bournel*[1,3]*, Stéphane Carniato*[1]*, Emmanuelle Dubois*[4]*, Laurent Michot*[4] *and Virginie Marry*[4]***

[1] Sorbonne Université, CNRS, Laboratoire de Chimie Physique Matière et Rayonnement (LCPMR), F-75005 Paris, France.

[2] Université de Lille, CNRS, Unité de Catalyse et de Chimie du Solide, UMR 8181, 59655 Villeneuve d'Ascq, France

[3] Synchrotron SOLEIL, L'Orme des Merisiers, Saint-Aubin, BP 48, F-91192 Gif-sur-Yvette, France

[4] Sorbonne Université, CNRS, Physicochimie des Electrolytes et Nanosystèmes Interfaciaux (PHENIX), F-75005 Paris, France.

*Corresponding authors: anthony.boucly@sorbonne-universite.fr; francois.rochet@sorbonne-universite.fr; virginie.marry@sorbonne-universite.fr

KEYWORDS. Clays, smectites, water, soft X-rays, synchrotron radiation, near ambient pressure, X-ray photoelectron spectroscopy, electronic structure, core-ionization spectroscopy, binding energy shifts, molecular dynamics, DFT quantum chemistry.

ABSTRACT

Utilizing Near Ambient Pressure X-ray Photoelectron Spectroscopy (NAP-XPS) under pressures up to 10 mbar, this study investigates the hydration behaviors of two swelling (negatively charged) smectite clays, specifically hydroxyhectorite and hydroxysaponite, under the influence of counterions, Cs^+, Na^+ and Sr^{2+} which differ in size and affinity for water. NAP-XPS reveals differences in the electronic structures of hydroxyhectorite and hydroxysaponite, which are related to the location of cation substitution within the negatively charged phyllosilicate layers. Importantly, this study provides atomic-scale insights into the interactions between water and these clays, focusing on changes in the counterion core-level binding energies due to hydration. We discuss the fact that the binding energy shift due to hydration results from the combination of two components: a physical component related to a change in the electrostatic potential (calculated after molecular dynamics simulation), and a chemical component related to a change in charge transfer between ligands and counterion, due to the replacement of phyllosilicate oxygen atoms with water molecules (as suggested by quantum chemistry calculations). These insights—critical for understanding the electronic structure of swelling smectites—open promising avenues for future research into the hydration mechanisms of other nanostructured minerals using NAP-XPS.

1. Introduction

Smectites are clay minerals where negatively charged phyllosilicate layers are stacked and separated by interlayer spaces containing with positive counterions. The unique characteristic of these minerals is their ability to absorb water (and other molecules) into the interlayer space, causing the clay to swell.[1] This property has garnered significant interest across various fields, including soil engineering,[2] nuclear waste storage, [3,4] nanofluidics, [5] and materials science, where the capability to insert molecules into the interlayer is particularly valued.[6]

Figure 1 illustrates the structure of smectites which are formed with two tetrahedral (T_h) silicon sheets sandwiching a central octahedral (O_h) magnesium oxide sheet, and thus smectites belong to the 2:1 or TOT clays family.[7] The layers acquire their negative charge from the isomorphic substitution of certain cations with lower valency ones in either the T_h or O_h sheets.[8] This negative charge is balanced by positive counterions (exchangeable cations) in the interlayer space. Additionally, the layer surface features siloxane rings with hexagonal cavities, which encapsulate hydroxyl groups from the O_h sheet.

The hydration state of swelling smectites is typically determined using X-ray diffraction (XRD) patterns measured under various relative humidity (RH).[9,10,11] These patterns allow measuring the basal spacing d_{001} and its evolution with RH. Commonly reported hydration states for smectites include dehydrated layers (0W, d_{001} in the 0.97–1.02 nm range), mono-hydrated layers (1W, d_{001} in the 1.16–1.29 nm range), bi-hydrated layers (2W, d_{001} in the 1.49–1.57 nm range), and tri-hydrated layers (3W, d_{001} in the 1.80-1.90 nm range). The interpretation of X-ray diffraction (XRD) profiles involves assumptions about the distribution of counterions and water planes, which may not always match the results of simulations.[12,13,14,15] For light counterions such as Na^+, whose scattering power is similar to that of water molecules, the refinement of their positions remains unaddressed.[16]

A key question arises regarding whether interlayer counterions assume inner-shell or outer-shell configurations depending on the clay's hydration state. Unfortunately, experimental data on the atomistic details of clay swelling are scarce. Until now, the application of Extended X-ray Absorption Fine Structure Spectroscopy (EXAFS) has been confined to 'dry' clays, despite its potential to provide valuable insights into this matter. [17,18]

Therefore, there is a pressing need for experimental data derived from techniques sensitive to chemical bonding. X-ray photoemission spectroscopy (XPS) is one such technique, though its application in studying clays has been minimal, with the notable exception of early work on dry clays by Ebina and coworkers[19] in the late 90s using ultra-high vacuum (UHV) monochromatized Al K_α XPS. At that time, the study of swelling clays using XPS was hindered by the water pressures in the mbar range and above. However, the introduction of near-ambient pressure XPS (NAP-XPS)[20,21,22,23,24,25,26,27] around two decades ago significantly transformed the landscape of surface science. NAP-XPS systems, capable of operating under pressures of up to approximately 10 mbar using soft X-ray, have enabled XPS experiments in environments with 100% RH at temperatures below approximately 7°C.

Previous research by the present authors provided initial insights into the effect of hydration on the electronic structure of clays, particularly on the counterion core-level binding energy, through the study of pyridine insertion into hydrated Sr^{2+}-hydroxyhectorite.[25] Despite its contributions, that study left the origins and extents of these effects largely unexplored. Therefore, the primary objective of the present research was to fully assess the potential of NAP-XPS core-level spectroscopy in monitoring in real time the interlayer hydration of synthetic hydroxyhectorite (with a per unit cell composition of $[\mathrm{X}_{0.8/z}]^{\mathrm{inter}}[\mathrm{Mg}_{5.2}\mathrm{Li}_{0.8}]^{\mathrm{O_h}}[\mathrm{Si}_{8.0}]^{\mathrm{T_h}}\mathrm{O}_{20}(\mathrm{OH})_4$)and synthetic hydroxysaponite (with a per unit cell composition of $[\mathrm{X}_{0.8/z}]^{\mathrm{inter}}[\mathrm{Mg}_6]^{\mathrm{O_h}}[\mathrm{Si}_{7.2}\mathrm{Al}_{0.8}]^{\mathrm{T_h}}\mathrm{O}_{20}(\mathrm{OH})_4$), where X represents a z-valent cation (X^{z+}).

Both the positioning of the substituting cation within the O_h or T_h sheets, and the characteristics of the exchangeable cation (size and charge) influence the swelling properties of clays.[10,11, 28,29,30,31,32,33] The phyllosilicate layers of hydroxyhectorite and hydroxysaponite possess the same negative charge density. However, in hydroxysaponite, the substitution of Si^{4+} with Al^{3+} occurs within the T_h sheet, whereas in hydroxyhectorite, the substitution of Mg^{2+} with Li^+ takes place in the O_h sheet. As a consequence, the negative charge spreads over the oxygen atoms on the surface of the phyllosilicate layers. It is more uniform for hydroxyhectorite and more localized on the oxygens bonded to Al^{3+} in the case of hydroxysaponite. In addition, the selected counterions, Cs^+, Na^+ and Sr^{2+} exhibit significantly different water affinities and ionic radii: the hydration enthalpy[34] of gaseous Cs^+, Na^+ and Sr^{2+} are –264, –406, and –1446 kJ/mol respectively; Sr^{2+} has a ionic radius of 132 pm, intermediate between that of Na^+ (116 pm) and that of Cs^+ (181 pm).[35] Therefore, by varying both the identity of the counterions and the location of the substituting cations in the phyllosilicate layer, we can anticipate observing a variety of changes in the electronic structures upon hydration.

This NAP-XPS study demonstrates that effects of hydration are manifested on the counterion core-level binding energies. The interpretation of these energy shifts was supported by molecular dynamics (MD) calculations. These calculations not only describe counterion coordination but also enable estimating variations in the electrostatic potential upon hydration, which significantly contributes to the initial-state shift. Additionally, quantum chemistry calculations were carried out to elucidate the changes in charge transfer from the ligand to the counterion associated with the replacement of phyllosilicate oxygens by water molecules, both in the ground state and core-ionized state. A combined effect of changes in electrostatic potential and counterion electron population is essential to explain the observed binding energy variations.

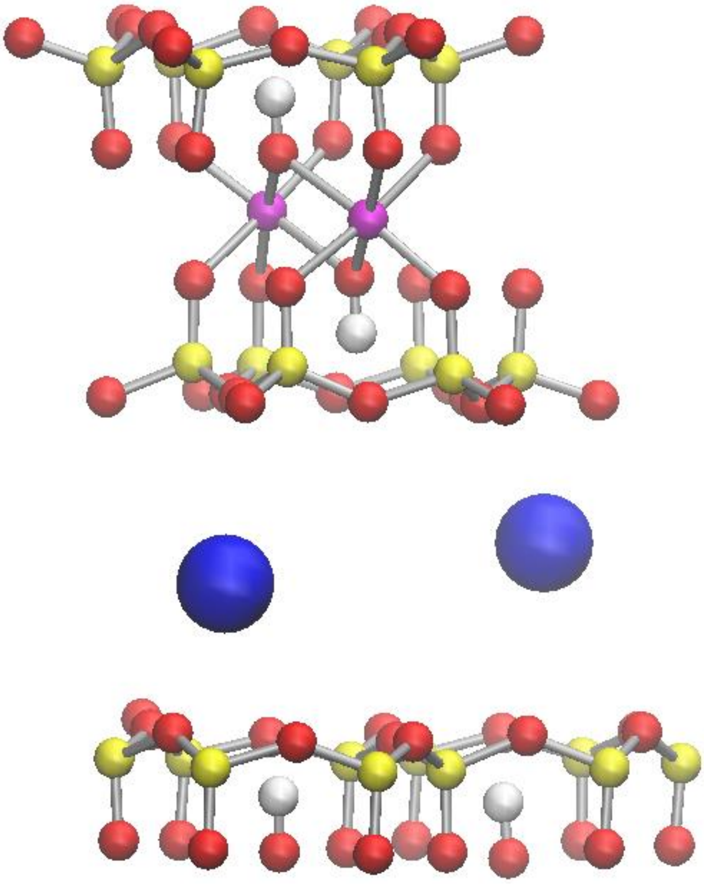

Figure 1. Smectite structure; red:O; blue: counterion; yellow:Si, magenta:Mg; white:H. In hydroxyhectorite Mg^{2+} is substituted by Li^{+}, while in hydroxysaponite, Si^{4+} is substituted by Al^{3+}.

2. METHODS

2.1. Molecular Dynamics Calculations

Molecular dynamics (MD) simulations were performed with the LAMMPS package.[36] Periodic boundary conditions were used in all directions. The simulation box contained three clay layers of hydroxylated hectorite, consequently three interlayer spaces. Each layer consisted of 50 unit cells of formula $[\mathrm{X}_{0.8/z}]^{\mathrm{inter}}[\mathrm{Mg}_{5.2}\mathrm{Li}_{0.8}]^{\mathrm{O_h}}[\mathrm{Si}_{8.0}]^{\mathrm{T_h}}\mathrm{O}_{20}(\mathrm{OH})_4)$ where X represents a z-valent cation (X^{z+}). (Na^{+}, Cs^{+} or Sr^{2+}). The chosen force field describing the interatomic forces was the clayFF forcefield[37] with SPCE water.[38] For Na, Cs and Sr, the parameters are respectively from refs [39],[40],[41]. The long-range electrostatic interactions were calculated using the Particle-Particle-Particle-Mesh solver with a precision of 10^{-4}. The short-range electrostatic and Lennard-Jones interactions were calculated up to a cutoff radius of 0.9 nm.

For the dry state (0W), the counterions were first allowed to move in the interlayer spaces by fixing the interlayer spacing at 1.15 nm. The Nose-Hoover thermostat was used for NVT simulations (fixed interlayer spacings) with a thermostat constant of 1 ps. The timestep was 1 fs. After an equilibration phase of 100 ps, the interlayer spacings were reduced to values close to known experimental values for dry interlayer spaces of hectorite or similar smectite clays: 0.97 nm for Na^{+}-hydroxyhectorite,[16,42] 1.07 nm for Cs^{+}-hydroxyhectorite[43] and 1.0 nm for Sr^{2+}-hydroxyhectorite.[29,44] After another equilibration phase, trajectories were recorded in NVT over a 200 ps simulation from which equilibrium properties were calculated.

For the monohydrated state (1W), 5 H_2O per counterion were added to the interlayer spaces. The interlayer spacing was fixed to 1.25 nm for the three clays. After an equilibration phase of 100 ps, trajectories were recorded over a 200 ps simulation from which equilibrium properties were calculated. A snapshot of the monohydrated state with Na^{+} as the counterion is given in Figure 2.

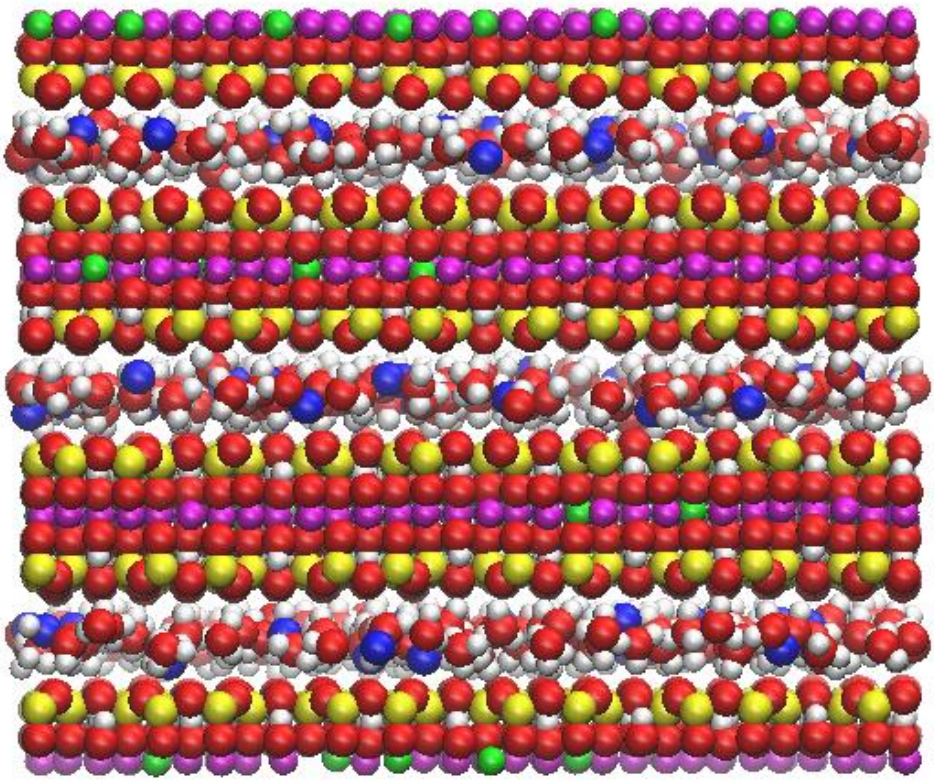

Figure 2. Snapshot of Na^+-hydroxyhectorite in the monohydrated (1W) state; red:O; blue: Na; yellow:Si, magenta:Mg; green: Li, white:H.

From these trajectories, radial distribution functions, coordination numbers and charge densities could be computed. They were also used to calculate the average electrostatic potential felt by Mg and the counterion, to calculate the potential difference between both which helps interpreting NAP-XPS experiments. The calculation was performed thanks to a home-made program using Ewald summation with a precision of 10^{-2}.

A modified clayFF forcefield[12] was also used to evaluated the sensitivity of the results to the size of the surface oxygen (which impacts the distance of the fluid to the surface). The results are not presented because they did not impact the results quantitatively. The sensitivity of the results to the interlayer spacings was also studied by performing simulations in NPzT ensemble, i.e. by letting the spaces evolve under a pressure perpendicular to the clay layers equal to 1 bar. This did not change the results significantly either. In the case of Cs-hectorite that hydrates less, simulations with 4 H_2O per counterion were also performed.

2.2 Quantum Chemistry Calculations

The simulation of the charge transfer process was conducted by utilizing two small clusters $[Na\text{-}H_2O]^+$ and $[Na\text{-}O]^-$. For the hydrated cluster geometry, optimization was performed using a small 6-311G* basis set for both sodium and the (O/H) ligands using the density functional theory (DFT) GAMESS(US) package[45] and applying the Becke[46] three-parameter hybrid exchange and the Lee-Yang-Parr[47] gradient-corrected correlation functional (B3LYP). For $[Na\text{-}O]^-$ the internuclear distance was fixed to 0.244 nm, the MD simulated value. The 6-311G* basis set designed for Na combined with DFT level of theory was also used for Na 2s core binding energy calculation. In order to take into account relaxation and differential correlation, Self-Consistent Field (SCF) iteration process was applied to take into account both relaxation and induced correlation effect in the core hole final state compared to the initial state. The clusters were "embedded" in a polarizable medium describing an aqueous solution, using the so-called polarizable continuum model (PCM) implemented in GAMESS(US), where the nonequilibrium model accounts for electronic relaxation only. Keeping electronic relaxation only (and excluding that of the nuclei) implies that the relative permittivities at infinite frequency in bulk water and clay minerals must be considered and compared. That of bulk water is 1.8,[48] while that of SiO_2 (a constituent of clays) is 2.[49] Therefore, the PCM approach is reasonable to calculate ionization energies in the present case.

The change of population analysis of the occupied molecular orbitals between the initial and final states was performed using the Löwdin[50] approach. Indeed, while the Mulliken population analyses is conceptually simple, it suffers from a heavy dependence on the basis set used, as well as from the possibility of producing unphysical negative numbers of electrons. The Löwdin population analysis is an alternative that does not present these drawbacks. It uses the Löwdin symmetrically orthogonalized basis set (which is still atom-tagged) to assign the electron density.

2.3. Clay Deposits

Clay films of ~ 1 μm thickness were deposited on a gold-coated silicon wafer by evaporating dilute aqueous suspensions of (i) synthetic hydoxyhectorite and (ii) synthetic hydroxysaponite exchanged with Cs^+ ,Sr^{2+} or Na^+ counterions.[10] The preparation of the clay dispersion solution used for drop-casting is available in ref[32].The platelets have typical dimensions of ~ 1 µm and micro-domains or tactoids are typically constituted of 20 platelets.[51] The platelets are laid flat on the gold substrate.[51–53]

2.4. Synchrotron Radiation NAP-XPS at TEMPO Beamline

The experiment was conducted at the NAP-XPS station located at the TEMPO beamline of SOLEIL synchrotron. It utilized a SPECS PHOIBOS NAP-XPS 150 analyzer for the measurements, see refs.[25,27] To maximize the photoelectron signal intensity, the analyzer aperture (a pinhole of diameter 0.3 mm) is brought close to the sample surface at a distance of ~1 mm. The analyzer acceptance cone, as given by the manufacturer, has an apex angle 2α of 44°. However, at a working distance of 1 mm the acceptance angle is reduced with respect to the latter value (a value of 32° is found for 2α assuming a point X-ray spot).

After introduction in the NAP-XPS analysis chamber, the clay sample underwent cooling via a Peltier cooler. The sample holder temperature, as measured by a thermocouple, was chosen between 1°C and 3°C. Ultra-pure water (degassed after several freeze-pump-thaw cycles) was subsequently introduced through a leak valve until the desired pressure (measured with a Baratron gauge) was attained. The experiment was terminated upon formation of liquid water on the sample surface, with the initial droplet formation monitored using a camera focused on the sample holder. At dewpoint, the pressure p_{dp} corresponds to 100% relative humidity (RH). The RH at pressures p lower than p_{dp} was calculated with the formula $\mathrm{RH} = \frac{p}{p_{dp}} \times 100\%$. As the pressure escalated, the signal emanating from the sample progressively diminished. Therefore, for spectrum comparison purposes, curves are multiplied by factors indicated in the figures.

The core-level spectra were recorded at photon energies of 750 and 1050 eV using a pass energy of 50 eV with slits of 3x20 mm corresponding to an analyzer resolution of 500 meV. Discussion about the difference in probing depth and its impact on the different contribution is available in SI section S2. In all figures presented in this article, the Mg 2p core-level is used as reference peak and its binding energy is fixed at a constant value to make the binding energy shifts of the counterion core-levels and of the Si 2p core-level more easily observable. Therefore, we will specifically consider changes in the binding energy difference $BE_{Mg\ 2p}^{CI\ CL} = BE(CI\ CL) - BE(Mg\ 2p)$ (where CI denotes counterion and CL core-level) that are related to the hydration process. Discussion about why Mg 2p was chosen as reference peak and charging effect observed during experiment is available in SI section S4. Spectra were fitted using Gaussian shape peaks and Shirley background. The spin-orbit splitting values are 2.3 eV for the Cs $4d_{3/2}/4d_{5/2}$ doublet, 1.8 eV for the Sr $3d_{3/2}/3d_{5/2}$ doublet, 0.6 eV for the Si $2p_{1/2}/2p_{3/2}$ doublet and 0.4 eV for the Al $2p_{1/2}/2p_{3/2}$ doublet. The branching intensity ratio of the spin-orbit split components of total angular momentum J_2 and J_1 is taken as $\frac{2J_2+1}{2J_1+1}$. Mg 2p was modeled with a single Gaussian component, owing to the small spin-orbit splitting of 0.28 eV.[54] Fitting parameters are collected in the Supporting Information (SI), section S1 (Tables S1 to S6). The possibility of radiolysis due to beam effect is discussed in SI section S5.

3. RESULTS AND DISCUSSIONS

3.1. MD Calculation of Counterion Environments in the 0W and 1W State and Electrostatic Potential (Hydroxyhectorite Case)

Pair distribution functions $g(r)$ can be calculated to get a more detailed picture of counterion environments in both the dry (0W) and monohydrated (1W) states. The positions of the first peak of the $g(r)$ function between counterions and oxygen are provided in Table 1. The coordination numbers n_{coord} are calculated as the integral of $g(r)$ according to:

$$n_{coord} = \rho \int_0^{r_c} 4\pi r^2 \, g(r) dr$$

where ρ is the density (the number of atoms per unit volume) and r_c the first minimum in the pair distribution function $g(r)$.

counterion/ hydration state	Atomic pair	1st peak position (nm)	r_c (nm)	n_{coord}	total n_{coord}
0W Na^+	Na-O_S	0.241	0.30	5.3	5.3
1W Na^+	Na-O_S	0.244	0.30	1.3	5.0
	Na-O_W	0.235	0.30	3.7	

0W Sr^{2+}	Sr-O_S	0.268	0.34	8	8
1W Sr^{2+}	Sr-O_S	0.270	0.34	2.5	7.9
	Sr-O_W	0.254	0.34	5.4	
0W Cs^+	Cs-O_S	0.329	0.42	12	12
1W Cs^+	Cs-O_S	0.326	0.42	7.1	11.4
	Cs-O_W	0.306	0.42	4.3	
all counterions	Mg-O	0.21	0.30	6	6

Table 1. Values of $g(r)$, r_c and n_{coord} obtained for Na^+, Sr^{2+} and Cs^+ hydroxyhectorite from MD calculations. In all cases the H_2O:counterion ratio was 5:1.

To compare the dry and hydrated states, the value of r_c (see Table 1) was chosen to be the same for both states and both oxygen types (O_S for surface oxygen atoms and O_W for water oxygen atoms). Fortunately, regardless of the hydration state and type of oxygen surrounding the counterion, the $g(r)$ minima are very close for a given clay. The $g(r)$ function and the coordination function are given in the SI, Figures S4 and S5.

Knowing the coordination of the counterion with oxygen neighbors may help to better apprehend the effects of hydration. Two parameters must be considered: the distance between the counterion and the surrounding oxygen atoms (the position of the first $g(r)$ peak in Table 1) and the number of oxygens in its first coordination sphere (n_{coord} also given in Table 1).

In the case of Na^+-hydroxyhectorite, the counterion-oxygen distance is short (about 0.24 nm) and the coordination number is low (~5) regardless of the hydration state (0W or 1W). For Sr^{2+}-hydroxyhectorite, the counterion-oxygen distance is also short (~0.26 nm), but n_{coord} is greater (~8) than for the smaller Na^+ ion. The n_{coord} value is also independent of the hydration state. For Cs^+-hydroxyhectorite, both in the 0W and 1W states, the counterion-oxygen distance (about 0.3-0.32 nm) is significantly larger than those obtained for the Na^+ - and Sr^{2+} -hydroxyhectorite. The n_{coord} value (~12), much greater that in the case of Na^+ and Sr^{2+}, is also practically independent of the hydration state.

From the MD atomic positions and charges, we calculate $V(x\ site)$ which stands for the electrostatic potential at the site where the atom x sits. Knowledge of $V(x\ site)$ is crucial to interpret changes in XPS binding energies (see below). It can be calculated by summing the electrostatic terms $\frac{Q_i}{4\pi\varepsilon_0 r_{xi}}$ over all atoms i different from x. Here, Q_i is the charge of atom i, and r_{xi} denotes the distance between x and atom i. From a methodological point of view, this sum contains long-range terms which can be calculated using the Ewald summation.[55] The electrostatic potential was calculated with a home-made code. The parameters used for the Ewald summation were chosen to yield a precision of 10^{-2} on $V(x\ site)$.

$V(CI\ site)$ and $V(Mg^{2+}\ site)$ are the electrostatic potentials (expressed in V) at the counterion (CI) site and at the Mg^{2+} site, respectively. We define $V_{Mg^{2+}\ site}^{CI\ site}$ as the potential difference between $V(CI\ site)$ and $V(Mg^{2+}\ site)$ ($V_{Mg^{2+}\ site}^{CI\ site} = V(CI\ site) - V(Mg^{2+})$). Calculated values of $V(CIsite)$, $V(Mg^{2+}\ site)$ and $V_{Mg^{2+}\ site}^{CI\ site}$ are reported in Table 2 for the 0W and 1W states in the case of hydroxyhectorite, and for the three counterions.

Counterion (CI)	Na^+		Sr^{2+}		Cs^+		
Hydration state	0W	1W $5H_2O$	0W	1W $5H_2O$	0W	1W $4H_2O$	1W $5H_2O$
$V(CIsite)$	–8.00	–9.32	–12.91	–14.72	–6.68	–7.06	–7.14
$\Delta V(CI\ site)$	-	–1.32	-	–1.81	-	–0.38	–0.46
$V(Mg^{2+}\ site)$	–15.76	–15.45	–15.47	–15.51	–15.74	–15.55	–15.50
$\Delta V(Mg^{2+}\ site)$	-	+0.31	-	–0.04	-	+0.19	+0.24
$V_{Mg^{2+}\ site}^{CI\ site}$	7.76	6.13	2.56	0.79	9.06	8.49	8.35
$\Delta V_{Mg^{2+}\ site}^{CI\ site}$	-	-1.63	-	-1.77	-	-0.57	-0.71

Table 2. Calculated values of $V(CI\ site)$, $V(Mg^{2+}\ site)$, and $V_{Mg^{2+}\ site}^{CI\ site}$ for Na^{+}, Sr^{2+} and Cs^{+} hydroxyhectorite. We also indicate the variation upon hydration of $V\ (x\ site)$, $\Delta V\ (x\ site)$, and of $V_{Mg^{2+}\ site}^{CI\ site}$, $\Delta V_{Mg^{2+}\ site}^{CI\ site}$. All values are in volts (V).

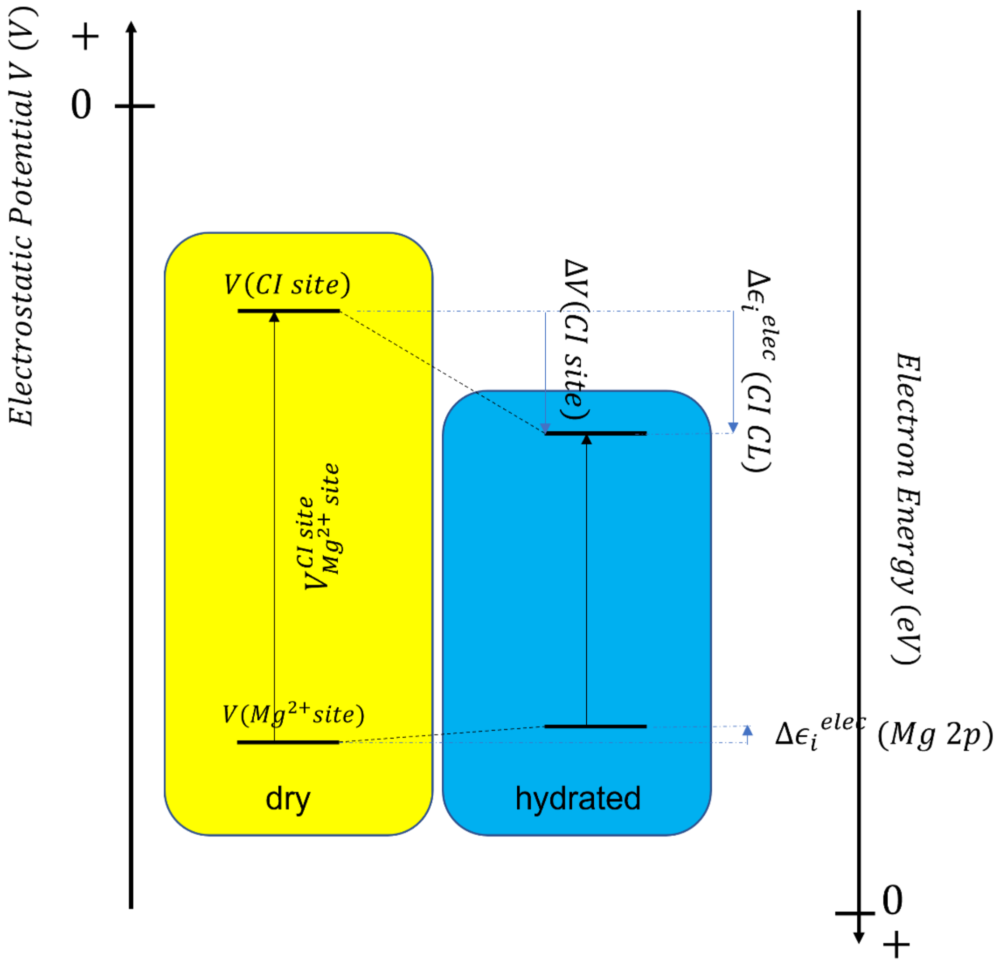

Figure 3. Schematic representation of the changes in the electrostatic potential (left axis in V units, directed upward) at the counterion and Mg^{2+} sites upon hydration, derived from MD calculation. The corresponding change in the energy of the electronic level i, ϵ_i (right axis in eV units, directed downward) is denoted as $\Delta \epsilon_i{}^{elec}$. The two axes are in opposite directions, as the electron energy is the product of $-e$ by the electrostatic potential V. As an initial-state effect, the electrostatic potential variation contributes by $-\Delta \epsilon_i{}^{elec}$ to the binding energy shift, see eqs 2 to 6.

Note that $V(CI\ site)$ is always greater than $V(Mg^{2+}\ site)$. This is not *a priori* surprising, given that Mg^{2+} sits in the negatively charged phyllosilicate layer, while the interlayer space where the counterion sits is positively charged on average. Upon hydration $V(Mg^{2+}\ site)$ varies little remaining within the interval of -0.04 V to +0.3 V. In contrast, $V(CI\ site)$ can see a sizeable decrease when water is added. The magnitude of its decrease is in the range of 1.3 V to 1.8 V interval for Na^+ and Sr^{2+}. For Cs^+, the decrease is smaller, ~0.4 V.

3.2. Core-Level Shift Analysis

Shifts (ΔBE) observed in the core-level binding energy of a given atom present in different chemical environments are typically interpreted in terms of initial and final-state contributions.[56] Within the framework of Hartree-Fock theory, the binding energy (BE) is written as:

$$BE = -\epsilon_i - E_R + \Delta E_c \qquad (1)$$

where ϵ_i is the energy of the orbital i ($\epsilon_i < 0$), E_R is the relaxation energy ($E_R > 0$), and ΔE_c is the variation in correlation energy. Between two different chemical environments, ϵ_i and E_R vary by $\Delta\epsilon_i$ and ΔE_R respectively, and the binding energy shift ΔBE is defined as:

$$\Delta BE = -\Delta\epsilon_i - \Delta E_R \qquad (2)$$

considering that $\Delta(\Delta E_c)$ is negligible.[56] The quantity $-\Delta\epsilon_i$ represents the so-called "initial-state contribution" to the binding energy shift and $-\Delta E_R$ the so-called "final-state contribution".

We now focus on the initial state contribution $-\Delta\epsilon_i$ to ΔBE. $\Delta\epsilon_i$ can be broken into two parts. The first part is related to a change in the electron population of the atom under consideration due to hydration. This part of $\Delta\epsilon_i$ can be denoted ${\Delta\epsilon_i}^{CT}$, where the superscript CT (for charge transfer) denotes a possible variation in the electronic population of the atom in its ground state upon hydration. This primarily affects the counterion, which experiences a change in the nature of its ligands. Indeed the (formally zero) occupation of the counterion ns orbital varies with the oxygen ligand, O_S or O_W, see the quantum chemistry computation below.

The second contribution to $\Delta\epsilon_i$, denoted $\Delta{\epsilon_i}^{elec}$, is associated to variations of the electrostatic potential, which displays, according to calculations, a significant variation upon hydration (more than 1 eV for Na^+ and Sr^{2+} counterions). $\Delta{\epsilon_i}^{elec}$ is similar to variations in band bending at semiconductor surfaces. [56] As shown in Figure 3, the core-level (CL) energy (in eV, axis oriented downward) at the counterion site changes by $\Delta{\epsilon_i}^{elec}\ (CI\ CL)$ which is equal to:

$$\Delta{\epsilon_i}^{elec}\ (CI\ CL) = -e\Delta V(CI\ site) \tag{3}$$

where e is the elementary charge ($e > 0$). For all three counterions $\Delta{\epsilon_i}^{elec}\ (CI\ CL)$ is positive (Table 2), thus the initial-state contribution $-\Delta{\epsilon_i}^{elec}\ (CI\ CL)$ to ΔBE is *negative*. Similarly, we obtain at the Mg^{2+} site:

$$\Delta{\epsilon_i}^{elec}\ (Mg\ 2p) = -e\Delta V(Mg^{2+}\ site) \tag{4}$$

Table 2 shows that $\Delta{\epsilon_i}^{elec}\ (Mg\ 2p)$ is negative for the Na^+ and Cs^+ counterions, and nearly zero for Sr^{2+}. In all cases $\left|\Delta{\epsilon_i}^{elec}\ (Mg\ 2p)\right| < \left|\Delta{\epsilon_i}^{elec}\ (CI\ CL)\right|$.

In practice, we use the Mg 2p binding energy as a reference, due to problematic charging issue. Therefore, we examine the variations of $BE_{Mg\ 2p}^{CI\ CL}$, $\Delta BE_{Mg\ 2p}^{CI\ CL}$:

$$\Delta BE_{Mg\ 2p}^{CI\ CL} = -\left(\Delta{\epsilon_i}^{elec}\ (CI\ CL) - \Delta{\epsilon_i}^{elec}\ (Mg\ 2p)\right) - \left(\Delta{\epsilon_i}^{CT}\ (CI\ CL) - \Delta{\epsilon_i}^{CT}\ (Mg\ 2p)\right) - \left(\Delta E_R(CI\ CL) - \Delta E_R(Mg\ 2p)\right) \tag{5}$$

which can be rewritten as:

$$\Delta BE_{Mg\ 2p}^{CI\ CL} = e\Delta V_{Mg^{2+}\ site}^{CI\ site} + \ (\Delta BE_{Mg\ 2p}^{CI\ CL})^{CT} \tag{6}$$

with $(\Delta BE_{Mg\ 2p}^{CI\ CL})^{CT} = -\Delta{\epsilon_i}^{CT}\ (CI\ CL) - \Delta E_R(CI\ CL) + \ \Delta{\epsilon_i}^{CT}\ (Mg\ 2p)\ + \Delta E_R(Mg\ 2p)$

Calculated $\Delta V_{Mg^{2+}\ site}^{CI\ site}$ values are reported in Table 2. Note that $e\Delta V_{Mg^{2+}\ site}^{CI\ site}$ is approximately equal to $-\Delta{\epsilon_i}^{elec}\ (CI\ CL)$, when $\left|\Delta{\epsilon_i}^{elec}\ (Mg\ 2p)\right|$ is significantly smaller than $\Delta{\epsilon_i}^{elec}\ (CI\ CL)$. This is clearly the case for the Na^+ and Sr^{2+} cations (see also Table 2).

Regarding $(\Delta BE_{Mg\ 2p}^{CI\ CL})^{CT}$ one can assume that $(\Delta BE_{Mg\ 2p}^{CI\ CL})^{CT} \approx -\Delta{\epsilon_i}^{CT}\ (CI\ CL) - \Delta E_R(CI\ CL)$ because $\Delta{\epsilon_i}^{CT}\ (Mg\ 2p)$ and $\Delta E_R(Mg\ 2p)$ vary little, as Mg^{2+} ions are nested in the middle of the phyllosilicate layer, and are much less sensitive to the presence of water molecules. This naturally limits the study to the hydration of the counter-ion, specifically to the replacement of O_S ligands by water molecules.

In this context, a DFT quantum chemistry approach limited to the cation and one ligand (an oxygen ion or a water molecule) can provide qualitative insights on $\Delta\epsilon_i{}^{CT}\ (CI\ CL)$ and $\Delta E_R\ (CI\ CL)$ upon hydration. Since the negative charge on the surface oxygen atoms (O_S) is about -1.05 (the charge used in clayFF, with the negative charge due to Mg^{2+} substitution by Li^+ evenly distributed over the O_S atoms in hydroxyhectorite), we considered two small clusters Na^+O^- and Na^+-H_2O to examine the effect of ligand substitution. The Löwdin electronic populations on the various atoms, in the ground state and the core ionized Na $2s^{-1}$ state, as well as those projected on particular orbitals are collected in Table S7 of the SI.

The calculation provides an ionization energy of Na^+-H_2O that is significantly greater (by +0.8 eV) than that of Na^+O^- (see Table S7). The population analysis helps in understanding why this is so. First, we note that in the ground state, the Löwdin electronic population of Na in Na^+-H_2O is less than in Na^+O^- (10.24 versus 10.31). Therefore, we expect that $-\Delta\epsilon_i{}^{CT}\ (CI\ CL)$ is positive.[56] Then, if we examine the variation in the electronic population in the Na $2s^{-1}$ state, 0.20 *(of* $-e$*)* is transferred from the ligand to (mostly) the Na 3s orbital in the Na $2s^{-1}$ state for Na^+O^-. The "O $2p_z$" isodensity map (z is the internuclear axis) has strongly changed, see Figure S6, extending over the sodium. For its part, Na^+-H_2O exhibits a much smaller ligand→Na charge transfer of 0.1 in the Na $2s^{-1}$ state (the charge is transferred to the Na 3s/3p/3d orbitals). Indeed, the $3a_1$ orbital of water is much less deformed towards the Na atom than the O $2p_z$ orbital of Na^+O^-, see Figure S6. We conclude that the screening of the Na 2s core-hole is significantly less effective when the ligand is a water molecule compared to when the ligand is an oxygen ion. Therefore, a positive $-\Delta E_R\ (CI\ CL)$ is expected. Hence, the binding energy increases when the oxygen ion is replaced by the water molecule.

Insights into the "real" smectite can be drawn from the DFT calculations applied to bimolecular clusters. The "complex" under consideration in clays consists of a Na^+ ion surrounded by approximately five ligands, either phyllosilicate layer oxygens O_S or water oxygens O_W. As our quantum chemistry calculation suggests, we expect that $(\Delta BE_{Mg\ 2p}^{CI\ CL})^{CT} \approx -\Delta\epsilon_i{}^{CT}\ (CI\ CL) - \Delta E_R(CI\ CL)$ will increase with an increasing number of water ligands substituting the O_S ligands. The *positive* $(\Delta BE_{Mg\ 2p}^{CI\ CL})^{CT}$ will counteract the *negative*

$e\Delta V^{CI\,site}_{Mg^{2+}\,site}$ in eq 6. Although this type of analysis was not extended to Sr^{2+} and Cs^{+} ions, insights from the Na^{+} case can be referenced in analyzing their core-level shifts.

3.3 NAP-XPS measurements

3.3.1 Cs^{+}-hydroxyhectorite and hydroxysaponite

The affinity of cesium ions for water is relatively limited. Sorption studies indicate that the d_{001} spacing for Cs^{+}-smectite remains within the range of 1.2 nm (equivalent to 1W) even at high RH[57–60] and after immersion in water.[57] Notably, less water is incorporated into the interlayer of Cs^{+}-smectites than in those with a small counterion like Na^{+}. In Cs^{+}-hydroxysaponite, the water/counterion ratio is ~3.75 while it is ~5 in Na^{+}-hydroxysaponite.[43] This is why we also tested the case of 4 H_2O/counterion in the MD calculation.

Figure 4 shows $BE^{Cs\,4d_{5/2}}_{Mg\,2p}$ plotted against RH for both Cs^{+}-hydroxyhectorite and Cs^{+}-hydroxysaponite. NAP-XPS spectra of the Cs 4d and Si 2p spectra are available in Figure S7 for Cs^{+}-hydroxyhectorite, and Figure S8 for Cs^{+}-hydroxysaponite. However, due to significant charging effects, the Cs 4d and Mg 2p spectra of Cs^{+}-hydroxyhectorite recorded in ultra-high vacuum (UHV) are omitted. Charging effects are already substantially reduced at 1.2 mbar (17% RH), rendering the spectra analyzable. For the same reasons, the Cs 4d and Mg 2p of Cs^{+}-hydroxysaponite are presented from a pressure of 2.5 mbar (35% RH).

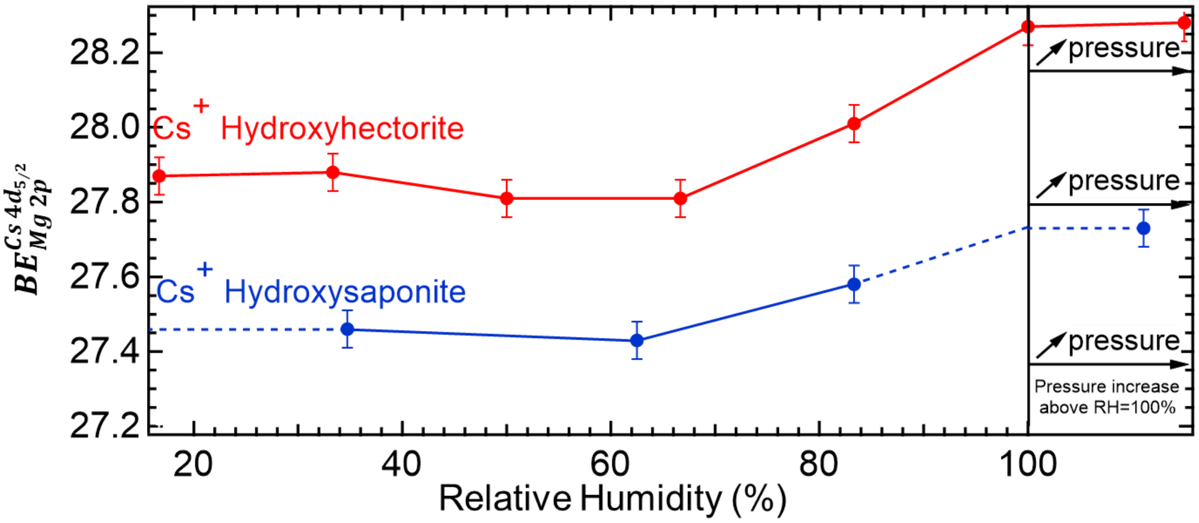

Figure 4. Plot of $\boldsymbol{BE_{Mg\ 2p}^{Cs\ 4d_{5/2}} = BE(Cs\ 4d_{5/2}) - BE(Mg\ 2p)}$ across different RH levels for Cs$^+$-hydroxyhectorite and Cs$^+$-hydroxysaponite. Note the systematically smaller $\boldsymbol{BE_{Mg\ 2p}^{Cs\ 4d_{5/2}}}$ value of Cs$^+$-hydroxysaponite (0.4 eV from 35% RH), reflecting the inherent structural differences between the two clay types.

$BE_{Mg\ 2p}^{Cs\ 4d_{5/2}}$ remains unchanged from 17% to 67% RH for Cs$^+$-hydroxyhectorite (only the XPS intensity diminishes as seen in Figure S7(a), due to the increased scattering of the photoelectrons by the gas phase). However, at 83% RH, $\Delta BE_{Mg\ 2p}^{Cs\ 4d_{5/2}}$ equals + 0.20 eV, then it reaches +0.4 eV at 100% RH. The measured shift is clearly related to the insertion of water in the interlayer. We recall that the calculated electrostatic initial-state contribution $e\Delta V_{Mg^{2+}\ site}^{Cs^+\ site}$ to the Cs 4d binding energy shift is negative upon formation of the 1W state, ranging from –0.71 eV (5H_2O/counterion) to –0.51 eV (4H_2O/counterion), see Table 2. As $\Delta BE_{Mg\ 2p}^{Cs\ 4d_{5/2}}$ is the sum of $e\Delta V_{Mg^{2+}\ site}^{Cs^+\ site}$ and $(\Delta BE_{Mg\ 2p}^{Cs\ 4d_{5/2}})^{CT}$ (eq 6), this means that $(\Delta BE_{Mg\ 2p}^{Cs\ 4d_{5/2}})^{CT}$ is *positive*, in the 0.9-1.1 eV range. The evolution of the Si $2p_{3/2}$ binding energy (relative to Mg 2p) $BE_{Mg\ 2p}^{Si\ 2p_{3/2}}$ as a function of RH also reveals an increase of + 0.23 eV at 100% RH (Table S1 and Figure S7).

As discussed in SI section 2, the Cs 4d signal encompasses contributions from counterions lying in the interlayers (estimated to 60%-75% of the spectral weight) and counterions sitting at the surface of the tactoids. In principle, different chemical environments[19] should lead to chemically shifted components. This is not seen experimentally as the Cs 4d spectra of both Cs$^+$-smectites (Figure S7(a) and S8(a)) are always fitted with a single spin-orbit split doublet. The Cs $4d_{5/2}$ FWHM in the case of Cs$^+$-hydroxyhectorite s is 1.76 eV (Table S1) under 1.2 mbar (17% RH). Under 2.4 mbar (34% RH), the Cs $4d_{5/2}$ FWHM is even smaller, 1.55 eV. These widths suggest that Cs$^+$ occupies rather equivalent sites, at least for water pressures ≥1.2 mbar.

In the case of Cs$^+$-hydroxysaponite, the Cs $4d_{5/2}$ component overlaps with the Al 2p peak (Al substitutes Si in the T_h sheets). However both signal can be easily deconvoluted (Figures S10(a,b)). Moreover, binding energy shifts can be visually appreciated via the Cs $4d_{3/2}$ component (Figure S8(a)). A single Cs 4d doublet is sufficient to fit the spectra and the FWHM remains stable at 1.58±0.03 eV with increasing RH indicating equivalent adsorption sites (e.g. surface and interlayer sites). Similar to Cs$^+$-hydroxyhectorite, Figures 4 shows that $\Delta BE_{Mg\ 2p}^{Cs\ 4d_{5/2}}$ is positive at high RH, reaching +0.30 eV at 100% RH. Although the electrostatic potential was not calculated for Cs$^+$-hydroxysaponite, it is very likely that the analysis made for hydroxyhectorite can also apply to this case. For its part, $BE_{Mg\ 2p}^{Si\ 2p_{3/2}}$, (Table S2, Figure S8(b) and Figure S10) increases by about +0.17 eV at 100% RH.

Finally, we see that X-ray photoelectron spectroscopy (XPS) is sensitive to differences in the electronic structures between hydroxyhectorite and hydroxysaponite. As illustrated in Figure 4, $BE_{Mg\ 2p}^{Cs\ 4d_{5/2}}$ is ~0.4 eV lower for Cs$^+$-hydroxysaponite compared to Cs$^+$-hydroxyhectorite.

3.3.2 Sr^{2+} hydroxyhectorite and hydroxysaponite

The alkaline-earth counterion Sr^{2+} has a high water hydration affinity (the gaseous hydration enthalpy[34] is -1446 kJ/mol) that drives the swelling of smectites.[61] However, it has been so far relatively little associated with hydroxyhectorite and hydroxysaponite in experimental studies. Hints from alkali-earth exchanged smectites indicate that Sr^{2+} hydroxyhectorite and hydroxysaponite should start to hydrate at low RH. The 1W state of Sr^{2+} montmorillonite already forms at 5% RH, and the 2W state occurs within the range of 35-40% RH.[62,29] Ca^{2+} saponite already reaches the 2W state at a RH of 20%, and the two-step hydration is difficult to observe.[9,10,30]

Figure 5 shows $BE_{Mg\ 2p}^{Sr\ 3d_{5/2}}$ is plotted against RH for both smectites. The individual Sr 3d spectra of Sr^{2+}-hydroxyhectorite acquired at hν=750 eV up to 48% RH are reported in Figure S11 while those of Sr^{2+-}hydroxysaponite acquired up to 100% RH are displayed in Figure S12. For Sr^{2+}-hydroxyhectorite, an initial decrease of $BE_{Mg\ 2p}^{Sr\ 3d_{5/2}}$ of 0.3 eV was observed at 2% RH (when the 1W state forms), in agreement with previous measurements,[25] and a subsequent minor one of 0.1 eV at RH=48%, when the 2W state is expected to form.[63] This leads to an overall decrease of 0.4 eV for $BE_{Mg\ 2p}^{Sr\ 3d_{5/2}}$ upon hydration, a shift opposite to that found for Cs$^+$. Note that the initial-state contribution of the electrostatic potential $e\Delta V_{Mg^{2+}\ site}^{Sr^{2+}\ site}$ to the Sr

3d$_{5/2}$ binding energy shift upon formation of the 1W state is negative −1.77 eV (see Table 2). This mean that $(\Delta BE_{Mg\ 2p}^{Sr\ 3d_{5/2}})^{CT}$ (eq 6) is *positive* and equals ~1.4 eV.

The Sr 3d spectra of Sr^{2+}-hydroxysaponite (Figure S12(a)) are well-resolved all the way from 0% RH to 100 % RH, due to the positive biasing of the sample holder and the use of "background" gas (Ar) at 0% RH (the FWHM remains in the 1.4-1.9 range). A significant $\Delta\ BE_{Mg\ 2p}^{Sr\ 3d_{5/2}}$ of –0.5 eV was observed between 2% and 15% RH (see Figure 5, and also Figure S12(a)) stronger than in hydroxyhectorite case. Beyond 35% RH up to 100%, i.e. in the 2W state, no further changes in $BE_{Mg\ 2p}^{Sr\ 3d_{5/2}}$ were observed. Figure S12(b) shows that the binding energy position of the Si 2p core level is remarkably constant with increasing RH, in contrast with the Cs^{+}-smectite case.

For both smectites, Sr 3d spectra are fitted with a single doublet, despite the fact that Sr^{2+} cations at the surface of the tactoids could represent 25 to 40% of the spectral weight at hν=750 eV indicating similar adsorption site for cations. Like for Cs^{+}- smectites, $BE_{Mg\ 2p}^{Sr\ 3d_{5/2}}$ for hydroxysaponite is ~0.4 eV lower than for hydroxyhectorite except at lower RH where the hydroxysaponite hydrates before the hydroxysaponite.

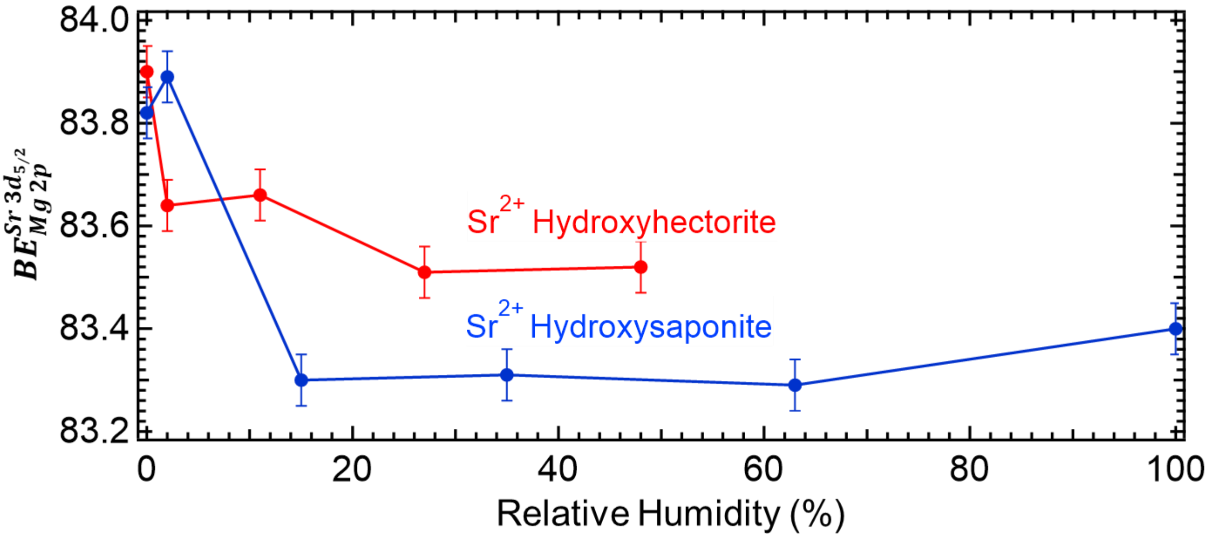

Figure 5. Plot of $\boldsymbol{BE_{Mg\ 2p}^{Sr\ 3d_{5/2}} = BE(Sr\ 3d_{5/2}) - BE(Mg\ 2p)}$ across different RH levels for Sr^{2+}-hydroxyhectorite and Sr^{2+}-hydroxysaponite. Note the smaller $\boldsymbol{BE_{Mg\ 2p}^{Sr\ 3d_{5/2}}}$ value of Sr^{2+}-

hydroxysaponite for RH>10%, reflecting the inherent structural differences between the two clay types.

Due to the significant swelling observed in smectites with a divalent counterion, it is reasonable to investigate whether a dilution of the Sr^{2+} ion could lead to its migration away from the surface or from the interlayer spaces. We define the cross-section corrected $\frac{I_{Sr\,3d}^{cor}}{I_{Mg\,2p}^{cor}}$ XPS intensity ratio as $\frac{I_{Sr\,3d}^{cor}}{I_{Mg\,2p}^{cor}} = \frac{I_{Sr\,3d}}{I_{Mg\,2p}} \times \frac{\sigma_{Mg\,2p}}{\sigma_{Sr\,3d}}$, where $\frac{I_{Sr\,3d}}{I_{Mg\,2p}}$ is the measured XPS intensity ratio and $\sigma_{Mg\,2p}$ ($\sigma_{Sr\,3d}$) is the Mg 2p (Sr 3d) cross-section at hν=750 eV.[64] If strontium and magnesium were homogeneously distributed in the depth of the sample, $\frac{I_{Sr\,3d}^{cor}}{I_{Mg\,2p}^{cor}}$ would be equal to the atomic ratio $\frac{[Sr]}{[Mg]}$, that is 0.075 for Sr^{2+}-hydroxyhectorite and 0.065 for Sr^{2+}-hydroxysaponite.

For Sr^{2+}-hydroxyhectorite, $\frac{I_{Sr\,3d}^{cor}}{I_{Mg\,2p}^{cor}}$ (see Figure 6) remains remarkably constant at ~0.04 up to 48% RH, indicating that that there is no loss of strontium up to this humidity level. However, this ratio is much lower than the nominal $\frac{[Sr]}{[Mg]}$ ratio, which is surprising. With a consistent density of strontium at the surface and within the layers, $\frac{I_{Sr\,3d}^{cor}}{I_{Mg\,2p}^{cor}}$ should be greater than the nominal $\frac{[Sr]}{[Mg]}$ ratio, as the signal of the Mg 2p photoelectrons is attenuated when crossing half the phyllosilicate layer and the external counterion layer. To explain this discrepancy, we could propose that the density of strontium is lower on the surface (by a factor of 1/2) than in the interlayer (a possibility discussed in section S2 of the SI). However, for Sr^{2+}-hydroxysaponite, Figure 6 shows that, at least for measurements made at RH>15%, the measured $\frac{I_{Sr\,3d}^{cor}}{I_{Mg\,2p}^{cor}}$ corresponds satisfactorily to the nominal $\frac{[Sr]}{[Mg]}$ ratio (~0.11) given the measurement accuracy, which suggests that, in this case, the counterion density is not depressed on the surface. Importantly, it also distinctly illustrates the absence of strontium loss up to 100% RH.

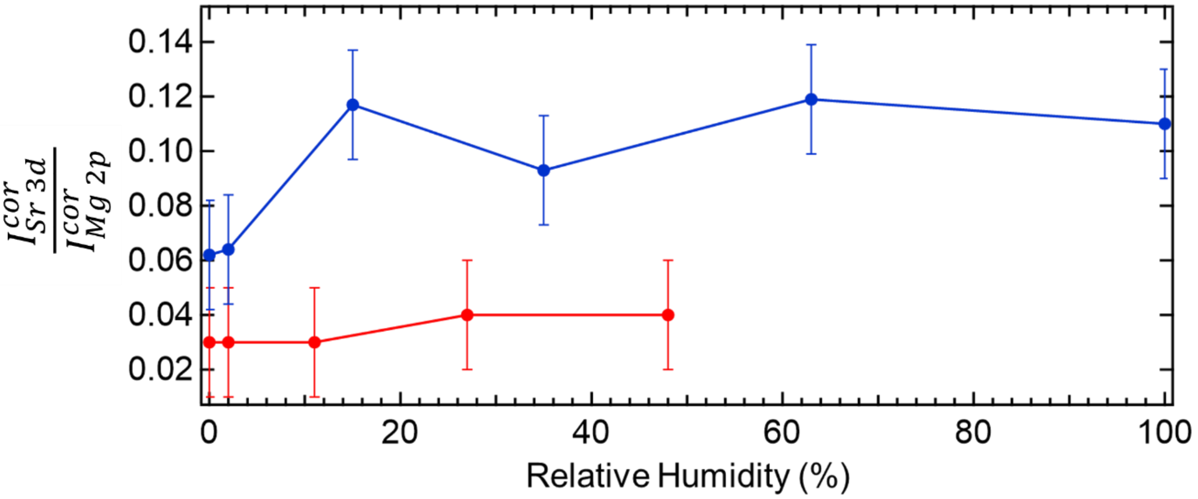

Figure 6. $\frac{I^{cor}_{Sr\,3d}}{I^{cor}_{Mg\,2p}} = \frac{I_{Sr\,3d}}{I_{Mg\,2p}} \times \frac{\sigma_{Mg\,2p}}{\sigma_{Sr\,3d}}$ intensity ratio as a function of RH for Sr^{2+}- hydroxysaponite (spectra acquired at hν=750 eV).

3.3.3 Na$^+$ hydroxyhectorite and hydroxysaponite

For Na$^+$ hydroxyhectorite and saponite the transition between the 1W state and the 2W state is clearly defined. Indeed, sorption and X-ray diffraction (XRD) studies demonstrate that for Na$^+$-hydroxyhectorite, the 1W state forms at low RH, specifically between 0% RH and 20% RH. Subsequently, the 2W state develops between approximately 40% RH and 60% RH.[16] The behavior of hydroxysaponite is remarkably similar, with the 1W state forming between 0% RH and 15% RH, and the 2W state appearing between 50% RH and 60% RH.[32]

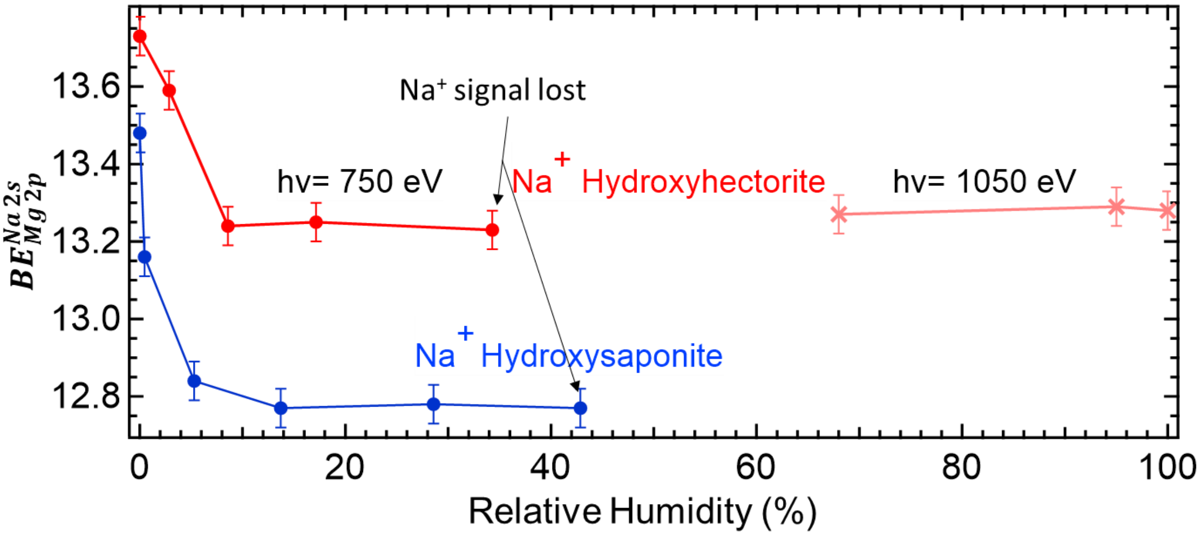

Figure 7. Plot of $\boldsymbol{BE_{Mg\,2p}^{Na\,2s} = BE(Na\,2s) - BE(Mg\,2p)}$ across different RH levels for Na$^+$-hydroxyhectorite and hydroxysaponite (circles for measurements at hν=750 eV, crosses for measurements at hν=1050 eV for hydroxyhectorite only). Note the systematically smaller $\boldsymbol{BE_{Mg\,2p}^{Na\,2s}}$ of Na$^+$-hydroxysaponite (0.4 eV smaller than that that types.of hydroxyhectorite for RH> 5%), reflecting the inherent structural differences between the two clay.

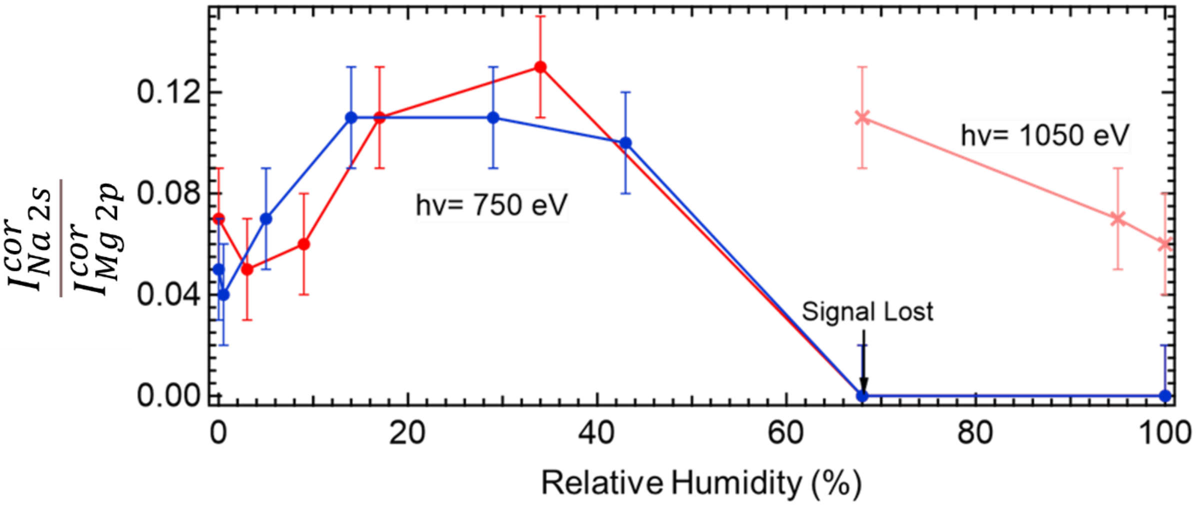

Figure 8. $\frac{I_{Na\,2s}^{cor}}{I_{Mg\,2p}^{cor}} = \frac{I_{Na\,2s}}{I_{Mg\,2p}} \times \frac{\sigma_{Mg\,2p}}{\sigma_{Na\,2s}}$ intensity ratio as a function of RH for Na$^+$-hydroxyhectorite (red circles) and Na$^+$-hydroxysaponite (blue circles) recorded at hν=750 eV. At this photon energy, the Na 2s signal is lost at RH=68% for both smectites. For Na$^+$-hydroxyhectorite the Na 2s signal is recovered at RH≥68% after displacing the measurement spot and using photons of 1050 eV energy (light red crosses).

Figure 7 shows $BE_{Mg\,2p}^{Na\,2s}$ plotted against RH for both Na$^+$-smectites. Individual NAP-XPS spectra of Na 2s and Mg 2p are shown in Figure S13 for Na$^+$-hydroxyhectorite, and Figure S14 for Na$^+$-hydroxysaponite. For Na$^+$-Hydroxyhectorite, $\Delta BE_{Mg\,2p}^{Na\,2s}$ (Figure 7) equals –0.5 eV upon hydration between 0% and 17% RH and then stabilizes up to RH=34%. At higher RH, the Na$^+$ signal is lost at hv=750 eV and can only be measured by increasing the photon energy to 1050 eV. The loss of sodium is discussed below. Similar observations can be made for the Na 2s spectra of Na$^+$-hydroxysaponite, (Figure 7) with an even larger shift in magnitude, $\Delta BE_{Mg\,2p}^{Na\,2s}$, is equal to –0.7 eV at 14% RH. This shift remains consistent up to 43% and is lost aferwards. For both smectites, Na 2s are fitted with a single component, despite the fact that Na^+ cations at the surface of the tactoids could represent 20 to 40% of the spectral weight. This is similar to the two previous counterion core-levels and indicates that adsorption sites are equivalent.

We recall that for hydroxyhectorite the initial-state contribution of the electrostatic potential $e\Delta V_{Mg^{2+}\,site}^{Na^+\,site}$ to the Na 2s binding energy shift upon formation of the 1W state is negative, –1.63 eV (see Table 2). Therefore, for Na^+-hydroxyhectorite, $(\Delta BE_{Mg\ 2p}^{Na\ 2s})^{CT}$ (eq 6) is *positive* and equals ~1.1 eV (hydroxyhectorite). A similar analysis should also apply for hydroxysaponite. For both Na^+-smectites, the (negative) sign and magnitude of the change in $BE_{Mg\ 2p}^{CI\ CL}$ are comparable to those observed in the case of Sr^{2+}-smectites, while contrasting with the positive $\Delta BE_{Mg\ 2p}^{CI\ CL}$ in Cs^+-smectites. However, at least for hydroxyhectorite for which calculations were made, everything is consistent when considering the $\Delta V_{Mg^{2+}\,site}^{CI\ site}$ values of Table 2. For the three counterions we have $\left|\Delta V_{Mg^{2+}\,site}^{CI\ site}\right|$ increasing in the Cs^+<Na^+<Sr^{2+} order (0.57, 1.63, 1.77, respectively) and positive values of $(\Delta BE_{Mg\ 2p}^{CI\ CL})^{CT}$ in the 0.9-1.4 eV range.

Additionally, $BE_{Mg\ 2p}^{Si\ 2p}$, which was consistently measured at the same photon energy only for Na^+-hydroxysaponite (Figure S14 (b)), was found to be particularly stable across the entire RH range from 0% to 100% RH (see Figure S9). This stability contrasts with the behavior seen in Cs^+-smectites. Like Cs^+-smectites and Sr^{2+}-smectites, Na^+-smectites also display a~0.4 eV difference for $BE_{Mg\ 2p}^{Na\ 2s}$ between Na^+-hydroxysaponite and to Na^+-hydroxyhectorite.

According to the literature, increasing the RH to 68% results in the formation of the 2W state for both Na^+-smectites.[16,32] Surprisingly, at this RH, the Na 2s signal vanishes from both Na^+-smectite spectra (Figures S13(a) and S14(a)) when measured at a photon energy of 750 eV. At 68% RH we are still far saturation, and, indeed, no water droplets are condensed on the Na^+-hydroxyhectorite surface (see picture, Figure S13(c)). Note also that the transition is abrupt. We plot in Figure 8, the cross-section corrected[64] $\frac{I_{Na\ 2s}^{cor}}{I_{Mg\ 2p}^{cor}}$ XPS intensity ratio. In the 20-40% RH range (1W state), $\frac{I_{Na\ 2s}^{cor}}{I_{Mg\ 2p}^{cor}}$ is constant at ~0.11 for both Na^+-smectites. Considering that the atomic ratio $\frac{[Na]}{[Mg]}$ is 0.15 for Na^+-hydroxyhectorite and 0.13 for Na^+-hydroxysaponite, the measured value of $\frac{I_{Na\ 2s}^{cor}}{I_{Mg\ 2p}^{cor}}$ is satisfactory (under the assumption of constant Na^+ density at the tactoid surface and in the interlayers). As there is no indication of Na 2s intensity loss with increasing RH in the 1W state, before the Na 2s signal disappearance at 64% RH, we interpret this observation as due to a considerable decrease of the Na^+ concentration at 68% RH when the 2W state forms.

To gain a better understanding of the phenomena, we analyzed a fresh area of the sample by moving the sample under the fixed analyzer nozzle of aperture 0.3 mm by 1 mm. We also increased the photon energy from 750 eV to 1050 eV, as the λ value of Na 2s/Mg 2p photoelectrons extends from ~2 nm to ~3 nm, allowing the probing of deeper layers. As seen Figure S13(a), the Na 2s core level reemerges. $BE_{Mg\ 2p}^{Na\ 2s}$ is still 13.30 eV, which means that in the 2W state the binding energy distance does not change relative to that of the 1W state, similar to the Sr^{2+}-smectite case. At 68% RH, the measured $\frac{I_{Na\ 2s}^{cor}}{I_{Mg\ 2p}^{cor}}$ was~ 0.11 after the first acquisition scan of ~10 min. However, in subsequent scans performed on the same spot, we observed that while the Mg 2p intensity remains constant, that of Na 2s continuously decreases with the number of acquisition scans (Figure S15). This indicates that the NAP-XPS measurement is the cause of the sodium loss. It also shows that further swelling due to measurement and corresponding counterion dilution cannot be assumed, as in such a case the Mg 2p signal would also decrease. At higher RH, the Na 2s signal is systematically recovered after the analysis spot is displaced (Figure 8).

Undoubtedly, the loss of sodium in Na^+ smectites results from two combined factors: (i) a high RH, which corresponds to the insertion of two or more water layers in the interlayer, and (ii) the NAP-XPS measurement itself. Regarding the first factor, it is important to note that similar counterion losses are not observed in Sr^{2+}-smectites in the 2W state. This behavior can be explained by the generally stronger bonding energies associated with divalent cations like Ca^{2+}, which prevent osmotic swelling—a phenomenon typical in Na^+ smectites—and restrict water insertion to crystalline swelling only.[65] As for the second factor, the specific mechanisms underlying the "measurement effect" remain elusive. The triggering effect may primarily be due to the X-ray beam. In this context, the monitoring of core-peak full width at half maximum (FWHM) values (Si 2p, Mg 2p, Al 2p) in Na^+-smectites does not indicate a significant increase at RH levels above 68%, which would typically suggest amorphization. Furthermore, concerning water radiolysis within the interlayers, although profound effects are observed in hydrated Sr^{2+}-hydroxyhectorite—such as the mineralization of inserted pyridine[25] —no counterion losses are detected. These findings underscore the need for additional research to fully understand these phenomena.

4. Conclusion

The present study highlights the capability of core-level NAP-XPS to monitor in situ (in the 10 mbar range) and in real time the changes in the electronic structure of hydroxyhectorite and hydroxysaponite due to their hydration. For Na^+ and Sr^{2+} smectites, counterion hydration was evidenced by shifts in Na 2s and Sr 3d binding energies to *lower* values (referenced to Mg 2p) already at relatively low RH, when the 1W state forms. However, no further change in binding energy was observed at high RH (2W state). Notably, for both Na^+-hydroxyhectorite and hydroxysaponite, the system was perturbed at high RH due to the combination of the 2W state formation and effects from NAP-XPS measurement, which led to the gradual loss of Na^+ ions. However, in the case of Sr^{2+} hydroxysaponite, the counterion concentration remained constant up to 100% RH. In stark contrast to the cases of Sr^{2+} and Na^+ smectites, Cs 4d shifts towards *higher* binding energies (referenced to Mg 2p) were observed in Cs^+-smectites when water penetrates the interlayer at high RH to form the 1W state. Unlike Na^+-smectites, but like Sr^{2+}-smectites, Cs^+ ions were not lost at high RH. Variations in the negative charge distribution in these two smectites are indicated by a lower binding energy of the counterion core-levels for hydroxysaponite compared to hydroxyhectorite, which demonstrates the high sensitivity of XPS to subtle differences on the electronic structure

The analysis of the core-level shifts was supported by MD calculations of the 0W and 1W states of hydroxyhectorite. MD provided insights into the coordination of counterions and the variation in the electrostatic potential due to hydration (swelling) at counterion and Mg^{2+} sites. This variation can be viewed as an initial-state contribution to the binding energy shift, akin to band bending variations at the surface of a semiconductor. Overlooking this contribution by focusing solely on a local “charge transfer with ligands” chemical analysis (we also performed complementary DFT quantum chemistry calculations to address this issue) could result in significant misinterpretations of the XPS data.

Calculations of the electrostatic potential in the 0W and 1W states of hydroxyhectorite reveal a *negative* initial-state contribution to the core-level binding energy shift upon hydration, common to all three counterions. Notably, the magnitude of this “physical” contribution is significantly larger for Na^+ and Sr^{2+} than for Cs^+. The addition of a “chemical” ligand-to-counterion charge transfer contribution, related to the substitution of the phyllosilicate oxygen ion ligands by water molecules, which is *positive* upon hydration–an effect supported by quantum chemistry calculations–, is explicative of the observed positive binding energy shift in the Cs^+-smectites. It also explains why the observed negative binding energy shift in Sr^{2+} and Na^+ smectites is significantly smaller than the magnitude of the calculated electrostatic potential variation.

In summary, NAP-XPS reveals how the complex interplay among clay platelets, counterions, and water molecules is reflected in the material's electronic structure. By monitoring the interlayer hydration of smectites at an atomic level, near-ambient pressure XPS core-level spectroscopy reveals its capacity to complement insights derived from molecular simulations. Evidently, this technique offers a promising avenue for further *in situ* exploration into the hydration mechanisms of other nanostructured minerals.

ASSOCIATED CONTENT

The Supporting Information is available free of charge via the Internet at http://pubs.acs.org.

Table S1: Cs $4d_{5/2}$, Mg 2p and Si $2p_{3/2}$ fitting parameters at hv=750 eV for Cs^+-hydroxyhectorite under various pressures.

Table S2: Cs $4d_{5/2}$, Mg 2p and Si $2p_{3/2}$ fitting parameters at hv=750 eV for Cs^+-hydroxysaponite under various pressures.

Table S3: Sr $3d_{5/2}$, Si $2p_{3/2}$ and Mg 2p fitting parameters at hv=750 eV for Sr^{2+}-hydroxyhectorite under various pressures.

Table S4: Sr $3d_{5/2}$, Si $2p_{3/2}$ and Mg 2p fitting parameters at hv=750 for Sr^{2+}-hydroxysaponite under various pressures.

Table S5: Na 2s and Mg 2p fitting parameters at hv=750 eV for Na^+-hydroxyhectorite under various pressures.

Table S6: Na 2s, Si $2p_{3/2}$ and Mg 2p fitting parameters at hν=750 eV for Na^+-hydroxysaponite under various pressures

Table S7. Löwdin population in the ground state and in the Na $2s^{-1}$ state for Na^+-O^- and Na^+-H_2O.

Figure S1. Cs^+-hydroxysaponite sample: evolution of the Mg 2p peak positions referenced to the Fermi level of the analyzer across increasing pressures.

Figure S2. C 1s peak of the Cs^+-hydroxyhectorite and their fitting.

Figure S3. Evolution of the C 1s C-C component binding energy with respect to the Fermi level of the analyzer as a function of the pressure for Cs^+- and Na^+-smectites.

Figure S4. The pair distribution functions $g(r)$ (solid line) in the dry state (0W) for Na^+, Sr^{2+} and Cs^+ hydroxyhectorite.

Figure S5. The pair distribution function $g(r)$ (solid line) in the monohydrated state (1W) for Na^+, Sr^{2+} and Cs^+ hydroxyhectorite.

Figure S6. Isodensity maps for the (a) Na^+-H_2O and (b) Na^+-O^- cluster, in the ground state and in the Na $2s^{-1}$ state.

Figure S7. Cs^+-hydroxyhectorite spectra measured at hν=750 eV for Cs 4d (a) and Mg 2p (b) for various RH, and Image of the sample under 7.2 mbar of water (c)

Figure S8. Cs^+-hydroxysaponite spectra measured at hν=750 eV for Cs 4d (a) and Mg 2p (b) for various RH.

Figure S9. $BE_{Mg\ 2p}^{Si\ 2p}$ versus RH for Cs^+-hydroxyhectorite, Cs^+-hydroxysaponite and Na^+-hydroxysaponite.

Figure S10. Cs^+-saponite spectra measured at hν=750 eV. Fitting of the Cs 4d and Al 2p binding energy region.

Figure S11. Sr^{2+}-hydroxysaponite spectra measured at hν=750 eV for Sr 3d and Mg 2p for various RH.

Figure S12. Sr^{2+}-hydroxysaponite spectra measured at hν=750 eV for Sr 3d and Mg 2p (a), and Si 2p (b) for various RH.

Figure S13. Na^{+}-hydroxyhectorite spectra measured at hν=750 eV for Na 2s and Mg 2p (a) for various RH, and Image of the sample under 4.8 mbar of water (b).

Figure S14. Na^{+}-hydroxysaponite spectra measured at hν=750 eV for Na 2s(b) and Mg 2p (a) for various RH.

Figure S15. Evolution of the Na 2s and Mg 2pcore level of the Na^{+}-hydroxyhectorite measured at hν=1050 eV at 68% RH with increased acquisition time.

AUTHOR INFORMATION

Anthony Boucly. Email: anthony.boucly@sorbonne-universite.fr

François Rochet. Email: francois.rochet@sorbonne-universite.fr

Virginie Marry. Email: virginie.marry@sorbonne-universite.fr

†Present address: TotalEnergies OneTech, F-69360 Solaize

AUTHOR CONTRIBUTION

Anthony Boucly: methodology of NAP-XPS experiments, NAP-XPS experiments, data analysis, writing–original draft.

François Rochet: fund raising (NAP-XPS setup), conceptualization and methodology of NAP-XPS experiments, validation of data analysis, writing – original draft.

Héloïse Tissot: methodology of NAP-XPS experiments, preliminary experiments and analysis, manuscript reading and editing.

Jean-Jacques Gallet: NAP-XPS station management and experiments, methodology of the NAP-XPS experiments, manuscript reading and editing.

Fabrice Bournel: NAP-XPS station management and experiments, methodology of the NAP-XPS experiments, manuscript reading and editing.

Quentin Arnoux: NAP-XPS experiments, manuscript reading and editing.

Stéphane Carniato. Core-ionized state calculations using advanced DFT quantum chemistry methods, manuscript reading and editing.

Emmanuelle Dubois: sample preparation, NAP-XPS experiments, manuscript reading and editing.

Laurent Michot: sample supply, sample preparation, NAP-XPS experiments, manuscript reading and editing.

Virginie Marry: sample preparation, NAP-XPS experiments, MD simulations and analysis, writing of the MD section, manuscript reading and editing.

All authors have given approval to the final version of the manuscript.

ACKNOWLEDGEMENTS

The NAP-XPS experiment, managed by the LCPMR team (Sorbonne Université), was funded by the Ile-de-France Region (Photoémission Environnementale en Ile-de-France, SESAME n°090003524), by the Agence Nationale de la Recherche (Surfaces under Ambient Pressure with Electron Spectroscopies, ANR- 08-BLAN-0096), and by Université Pierre et Marie Curie (now Sorbonne Université). Synchrotron SOLEIL supported the integration of the setup to TEMPO beamline. The authors thank warmly the TEMPO beamline staff for their efficient assistance. Anthony Boucly thanks Région Ile de France for his PhD grant HORS DIM EAU. The work was also partly supported by Labex MiChem.

References

(1) Hensen, E. J. M.; Smit, B. Why Clays Swell. *J. Phys. Chem. B* **2002**, *106* (49), 12664–12667. https://doi.org/10.1021/jp0264883.

(2) Anderson, R. L.; Ratcliffe, I.; Greenwell, H. C.; Williams, P. A.; Cliffe, S.; Coveney, P. V. Clay Swelling — A Challenge in the Oilfield. *Earth-Science Rev.* **2010**, *98* (3–4), 201–216. https://doi.org/10.1016/j.earscirev.2009.11.003.

(3) Bergaya F, Theng BKG, L. G. *Handbook of Clay Science*; Elsevier, 2006.

(4) Cattant, F.; Crusset, D.; F??ron, D. Corrosion Issues in Nuclear Industry Today. *Mater. Today* **2008**, *11* (10), 32–37. https://doi.org/10.1016/S1369-7021(08)70205-0.

(5) Shao, J.-J.; Raidongia, K.; Koltonow, A. R.; Huang, J. Self-Assembled Two-Dimensional Nanofluidic Proton Channels with High Thermal Stability. *Nat. Commun.* **2015**, *6*, 7602. https://doi.org/10.1038/ncomms8602.

(6) Suter, J. L.; Groen, D.; Coveney, P. V. Chemically Specific Multiscale Modeling of Clay-Polymer Nanocomposites Reveals Intercalation Dynamics, Tactoid Self-Assembly and Emergent Materials Properties. *Adv. Mater.* **2015**, *27* (6), 966–984. https://doi.org/10.1002/adma.201403361.

(7) Wyckoff, R. W. G. *Crystal Structures, Vol. 4*; John Wiley and Sons, New York, London, 1968.

(8) Odom, I. E. E. Smectite Clay Minerals: Properties and Uses. *Philos. Trans. R. Soc. London. Ser. A, Math. Phys. Sci.* **1984**, *311* (1517), 391–409.

(9) Watanabe, T.; Sato, T. Expansion Characteristics of Montmorillonite and Saponite Under Various Relative Humidity Conditions. *Clay Sci.* **1988**, *7*, 129–138.

(10) Karmous, M. S.; Ben Rhaiem, H.; Robert, J. L.; Lanson, B.; Ben Haj Amara, a. Charge Location Effect on the Hydration Properties of Synthetic Saponite and Hectorite Saturated by Na+, Ca2+ Cations: XRD Investigation. *Appl. Clay Sci.* **2009**, *46* (1), 43–50. https://doi.org/10.1016/j.clay.2009.07.007.

(11) Ferrage, E.; Lanson, B.; Michot, L. J.; Robert, J.-L. Hydration Properties and Interlayer

Organization of Water and Ions in Synthetic Na-Smectite with Tetrahedral Layer Charge. Part 1. Results from X-Ray Diffraction Profile Modeling. *J. Phys. Chem. C* **2010**, *114* (10), 4515–4526. https://doi.org/10.1021/jp909860p.

(12) Ferrage, E.; Sakharov, B. A.; Michot, L. J.; Delville, A.; Bauer, A.; Lanson, B.; Grangeon, S.; Frapper, G.; Jiménez-Ruiz, M.; Cuello, G. J. Hydration Properties and Interlayer Organization of Water and Ions in Synthetic Na-Smectite with Tetrahedral Layer Charge. Part 2. Toward a Precise Coupling between Molecular Simulations and Diffraction Data. *J. Phys. Chem. C* **2011**, *115* (5), 1867–1881. https://doi.org/10.1021/jp105128r.

(13) Ferrage, E.; Lanson, B.; Malikova, N.; Plançon, A.; Sakharov, B. A.; Drits, V. A. New Insights on the Distribution of Interlayer Water in Bi-Hydrated Smectite from X-Ray Diffraction Profile Modeling of 00 l Reflections. *Chem. Mater.* **2005**, *17* (13), 3499–3512. https://doi.org/10.1021/cm047995v.

(14) Tesson, S.; Louisfrema, W.; Salanne, M.; Boutin, A.; Ferrage, E.; Rotenberg, B.; Marry, V. Classical Polarizable Force Field To Study Hydrated Charged Clays and Zeolites. *J. Phys. Chem. C* **2018**, *122* (43), 24690–24704. https://doi.org/10.1021/acs.jpcc.8b06230.

(15) Hånde, R.; Ramothe, V.; Tesson, S.; Dazas, B.; Ferrage, E.; Lanson, B.; Salanne, M.; Rotenberg, B.; Marry, V. Classical Polarizable Force Field to Study Hydrated Hectorite: Optimization on DFT Calculations and Validation against XRD Data. *Minerals* **2018**, *8* (5), 205. https://doi.org/10.3390/min8050205.

(16) Dazas, B.; Lanson, B.; Breu, J.; Robert, J.-L.; Pelletier, M.; Ferrage, E. Smectite Fluorination and Its Impact on Interlayer Water Content and Structure: A Way to Fine Tune the Hydrophilicity of Clay Surfaces? *Microporous Mesoporous Mater.* **2013**, *181*, 233–247. https://doi.org/10.1016/j.micromeso.2013.07.032.

(17) Bostick, B. C.; Vairavamurthy, M. A.; Karthikeyan, K. G.; Chorover, J. Cesium Adsorption on Clay Minerals: An EXAFS Spectroscopic Investigation. *Environ. Sci. Technol.* **2002**, *36* (12), 2670–2676. https://doi.org/10.1021/es0156892.

(18) Honda, M.; Shimoyama, I.; Okamoto, Y.; Baba, Y.; Suzuki, S.; Yaita, T. X-Ray Absorption

Fine Structure at the Cesium L 3 Absorption Edge for Cesium Sorbed in Clay Minerals. *J. Phys. Chem. C* **2016**, *120* (10), 5534–5538. https://doi.org/10.1021/acs.jpcc.5b12378.

(19) Ebina, T.; Iwasaki, T.; Onodera, Y.; Chatterjee, A. A Comparative Study of DFT and XPS with Reference to the Adsorption of Caesium Ions in Smectites. *Comput. Mater. Sci.* **1999**, *14* (1–4), 254–260.

(20) Ogletree, D. F.; Bluhm, H.; Lebedev, G.; Fadley, C. S.; Hussain, Z.; Salmeron, M. A Differentially Pumped Electrostatic Lens System for Photoemission Studies in the Millibar Range. *Rev. Sci. Instrum.* **2002**, *73* (11), 3872. https://doi.org/10.1063/1.1512336.

(21) Bluhm, H. Photoelectron Spectroscopy of Surfaces under Humid Conditions. *J. Electron Spectros. Relat. Phenomena* **2010**, *177* (2–3), 71–84. https://doi.org/10.1016/j.elspec.2009.08.006.

(22) Salmeron, M.; Schlogl, R. Ambient Pressure Photoelectron Spectroscopy: A New Tool for Surface Science and Nanotechnology. *Surf. Sci. Rep.* **2008**, *63* (4), 169–199. https://doi.org/10.1016/j.surfrep.2008.01.001.

(23) Tissot, H.; Olivieri, G.; Gallet, J.-J.; Bournel, F.; Silly, M. G.; Sirotti, F.; Rochet, F. Cation Depth-Distribution at Alkali Halide Aqueous Solution Surfaces. *J. Phys. Chem. C* **2015**, *119* (17), 9253–9259. https://doi.org/10.1021/jp512695c.

(24) Tissot, H.; Gallet, J.-J.; Bournel, F.; Olivieri, G.; Silly, M. G.; Sirotti, F.; Boucly, A.; Rochet, F. The Electronic Structure of Saturated NaCl and NaI Solutions in Contact with a Gold Substrate. *Top. Catal.* **2016**, *59* (5–7), 605–620. https://doi.org/10.1007/s11244-015-0530-6.

(25) Boucly, A.; Rochet, F.; Arnoux, Q.; Gallet, J.-J.; Bournel, F.; Tissot, H.; Marry, V.; Dubois, E.; Michot, L. Soft X-Ray Heterogeneous Radiolysis of Pyridine in the Presence of Hydrated Strontium-Hydroxyhectorite and Its Monitoring by Near-Ambient Pressure Photoelectron Spectroscopy. *Sci. Rep.* **2018**, *8* (1), 6164. https://doi.org/10.1038/s41598-018-24329-8.

(26) Coustel, R.; Boucly, A.; Andre, E.; Di Bitetto, A.; Bournel, F.; Gallet, J.-J.; Rochet, F.; Carteret, C. NAP-XPS Probes the Electronic Structure of the Mg–Al–Cl Layered Double Hydroxide upon Controlled Hydration. *J. Phys. Chem. C 127* (8), 4144–4153. https://doi.org/10.1021/acs.jpcc.2c05362.

(27) Tissot, H.; Coustel, R.; Rochet, F.; Boucly, A.; Carteret, C.; André, E.; Bournel, F.; Gallet, J.-J. Deciphering Radiolytic Oxidation in Halide Aqueous Solutions: A Pathway Toward Improved Synchrotron NAP-XPS Analysis. *J. Phys. Chem. C* **2023**, *127* (32), 15825–15838. https://doi.org/10.1021/acs.jpcc.3c03676.

(28) Ikeda, T.; Suzuki, S.; Yaita, T. Characterization of Adsorbed Alkali Metal Ions in 2:1 Type Clay Minerals from First-Principles Metadynamics. *J. Phys. Chem. A* **2015**, *119* (30), 8369–8375. https://doi.org/10.1021/acs.jpca.5b05934.

(29) Ferrage, E. Investigation of Smectite Hydration Properties by Modeling Experimental X-Ray Diffraction Patterns: Part I. Montmorillonite Hydration Properties. *Am. Mineral.* **2005**, *90* (8–9), 1358–1374. https://doi.org/10.2138/am.2005.1776.

(30) Suquet, H.; Calle, C. D. E. L. a; Pezerat, H.; Jussieu, P. Swelling and Structural Organization of Saponite. *Clays Clay Miner.* **1975**, *23*, 1–9. https://doi.org/10.1346/CCMN.1975.0230101.

(31) Michot, L. J.; Villiéras, F.; François, M.; Bihannic, I.; Pelletier, M.; Cases, J.-M. Water Organisation at the Solid–Aqueous Solution Interface. *Comptes Rendus Geosci.* **2002**, *334* (9), 611–631. https://doi.org/10.1016/S1631-0713(02)01801-1.

(32) Michot, L. J.; Bihannic, I.; Pelletier, M.; Rinnert, E.; Robert, J. L. Hydration and Swelling of Synthetic Na-Saponites: Influence of Layer Charge. *Am. Mineral.* **2005**, *90* (1), 166–172. https://doi.org/10.2138/am.2005.1600.

(33) Rotenberg, B. Water in Clay Nanopores. *MRS Bull.* **2014**, *39* (12), 1074–1081. https://doi.org/10.1557/mrs.2014.251.

(34) Smith, D. W. Ionic Hydration Enthalpies. *J. Chem. Educ.* **1977**, *54* (9), 540. https://doi.org/10.1021/ed054p540.

(35) Shannon, R. D. Revised Effective Ionic Radii and Systematic Studies of Interatomic

Distances in Halides and Chalcogenides. *Acta Crystallogr. Sect. A* **1976**, *32* (5), 751–767. https://doi.org/10.1107/S0567739476001551.

(36) Thompson, A. P.; Aktulga, H. M.; Berger, R.; Bolintineanu, D. S.; Brown, W. M.; Crozier, P. S.; in ’t Veld, P. J.; Kohlmeyer, A.; Moore, S. G.; Nguyen, T. D.; et al. LAMMPS - a Flexible Simulation Tool for Particle-Based Materials Modeling at the Atomic, Meso, and Continuum Scales. *Comput. Phys. Commun.* **2022**, *271*, 108171. https://doi.org/10.1016/j.cpc.2021.108171.

(37) Cygan, R. T.; Liang, J.-J.; Kalinichev, A. G. Molecular Models of Hydroxide, Oxyhydroxide, and Clay Phases and the Development of a General Force Field. *J. Phys. Chem. B* **2004**, *108* (4), 1255–1266. https://doi.org/10.1021/jp0363287.

(38) Berendsen, H. J. C.; Grigera, J. R.; Straatsma, T. P. The Missing Term in Effective Pair Potentials. *J. Phys. Chem.* **1987**, *91* (24), 6269–6271. https://doi.org/10.1021/j100308a038.

(39) Smith, D. E.; Dang, L. X. Computer Simulations of NaCl Association in Polarizable Water. *J. Chem. Phys.* **1994**, *100* (5), 3757. https://doi.org/10.1063/1.466363.

(40) Smith, D. E.; Dang, L. X. Computer Simulations of Cesium–Water Clusters: Do Ion–Water Clusters Form Gas-Phase Clathrates? *J. Chem. Phys.* **1994**, *101* (9), 7873–7881. https://doi.org/10.1063/1.468213.

(41) Åqvist, J. Ion-Water Interaction Potentials Derived from Free Energy Perturbation Simulations. *J. Phys. Chem.* **1990**, *94* (21), 8021–8024. https://doi.org/10.1021/j100384a009.

(42) Bowers, G. M.; Singer, J. W.; Bish, D. L.; Kirkpatrick, R. J. Alkali Metal and H 2 O Dynamics at the Smectite/Water Interface. *J. Phys. Chem. C* **2011**, *115* (47), 23395–23407. https://doi.org/10.1021/jp2072167.

(43) Dzene, L.; Verron, H.; Delville, A.; Michot, L. J.; Robert, J.-L.; Tertre, E.; Hubert, F.; Ferrage, E. Influence of Tetrahedral Layer Charge on the Fixation of Cesium in Synthetic Smectite. *J. Phys. Chem. C* **2017**, *121* (42), 23422–23435. https://doi.org/10.1021/acs.jpcc.7b06308.

(44) Cases, J. M.; Bérend, I.; François, M.; Uriot, J. P.; Michot, L. J.; Thomas, F. Mechanism of Adsorption and Desorption of Water Vapor by Homoionic Montmorillonite: 3. The Mg2+, Ca2+, Sr2+ and Ba2+ Exchanged Forms. *Clays Clay Miner.* **1997**, *45* (1), 8–22. https://doi.org/10.1346/CCMN.1997.0450102.

(45) Schmidt, M. W.; Baldridge, K. K.; Boatz, J. A.; Elbert, S. T.; Gordon, M. S.; Jensen, J. H.; Koseki, S.; Matsunaga, N.; Nguyen, K. A.; Su, S.; et al. General Atomic and Molecular Electronic Structure System. *J. Comput. Chem.* **1993**, *14* (11), 1347–1363. https://doi.org/10.1002/jcc.540141112.

(46) Becke, A. D. Density-Functional Thermochemistry. III. The Role of Exact Exchange. *J. Chem. Phys.* **1993**, *98* (7), 5648. https://doi.org/10.1063/1.464913.

(47) Lee, C.; Yang, W.; Parr, R. G. Development of the Colle-Salvetti Correlation-Energy Formula into a Functional of the Electron Density. *Phys. Rev. B* **1988**, *37* (2), 785–789. https://doi.org/10.1103/PhysRevB.37.785.

(48) Hale, G. M.; Querry, M. R. Optical Constants of Water in the 200-Nm to 200-Mm Wavelength Region. *Appl. Opt.* **1973**, *12* (3), 555. https://doi.org/10.1364/AO.12.000555.

(49) Giustino, F.; Umari, P.; Pasquarello, A. Dielectric Discontinuity at Interfaces in the Atomic-Scale Limit: Permittivity of Ultrathin Oxide Films on Silicon. *Phys. Rev. Lett.* **2003**, *91* (26 I), 2676011–2676014. https://doi.org/10.1103/physrevlett.91.267601.

(50) Löwdin, P.-O. On the Non-Orthogonality Problem Connected with the Use of Atomic Wave Functions in the Theory of Molecules and Crystals. *J. Chem. Phys.* **1950**, *18* (3), 365–375. https://doi.org/10.1063/1.1747632.

(51) Porion, P.; Warmont, F.; Faugère, A. M.; Rollet, A.-L.; Dubois, E.; Marry, V.; Michot, L. J.; Delville, A. 133 Cs Nuclear Magnetic Resonance Relaxometry as a Probe of the Mobility of Cesium Cations Confined within Dense Clay Sediments. *J. Phys. Chem. C* **2015**, *119* (27), 15360–15372. https://doi.org/10.1021/acs.jpcc.5b03880.

(52) Cadene, A.; Durand-Vidal, S.; Turq, P.; Brendle, J. Study of Individual Na-Montmorillonite Particles Size, Morphology, and Apparent Charge. *J. Colloid Interface*

Sci. **2005**, *285* (2), 719–730. https://doi.org/10.1016/j.jcis.2004.12.016.

(53) Vantelon, D.; Belkhou, R.; Bihannic, I.; Michot, L. J.; Montargès-Pelletier, E.; Robert, J. L. An XPEEM Study of Structural Cation Distribution in Swelling Clays. I. Synthetic Trioctahedral Smectites. *Phys. Chem. Miner.* **2009**, *36* (10), 593–602. https://doi.org/10.1007/s00269-009-0304-4.

(54) Citrin, P. H.; Wertheim, G. K.; Baer, Y. Many-Electron Effects in Core-Level X-Ray and Electron Spectroscopies from Na, Mg, and Al. *Phys. Rev. Lett.* **1975**, *35* (13), 885–888.

(55) *Understanding Molecular Simulation*; Elsevier, 2002. https://doi.org/10.1016/b978-0-12-267351-1.x5000-7.

(56) Egelhoff, W. F. Core-Level Binding-Energy Shifts at Surfaces and in Solids. *Surf. Sci. Rep.* **1987**, *6* (6–8), 253–415. https://doi.org/10.1016/0167-5729(87)90007-0.

(57) MacEwan, D. M. C.; Wilson, M. J. Interlayer and Intercalation Complexes of Clay Minerals. *Cryst. Struct. clay Miner. their X-ray Identif.* **1980**, *5*, 197–248.

(58) Calvet, R. Water Aadsorption On Clays-Study OF Hydration Of Montmorillonite. *Bull. Soc. Chim. Fr.* **1972**, No. 8, 3097.

(59) Mooney, R. W.; Keenan, A. G.; Wood, L. A. Adsorption of Water Vapor by Montmorillonite. II. Effect of Exchangeable Ions and Lattice Swelling as Measured by X-Ray Diffraction. *J. Am. Chem. Soc.* **1952**, *74* (6), 1371–1374. https://doi.org/10.1021/ja01126a002.

(60) Prost, R. Interactions between Adsorbed Water Molecules and the Structure of Clay Minerals: Hydration Mechanism of Smectites. In *Proc. 5th Int. Clay Conf., Mexico City*; 1975; p 353.

(61) Salles, F.; Douillard, J.-M.; Bildstein, O.; Gaudin, C.; Prelot, B.; Zajac, J.; Van Damme, H. Driving Force for the Hydration of the Swelling Clays: Case of Montmorillonites Saturated with Alkaline-Earth Cations. *J. Colloid Interface Sci.* **2013**, *395*, 269–276. https://doi.org/10.1016/j.jcis.2012.12.050.

(62) Hendricks, S. B.; Nelson, R. a.; Alexander, L. T. Hydration Mechanism of the Clay

Mineral Montmorillonite Saturated with Various Cations [1]. *J. Am. Chem. Soc.* **1940**, *62* (6), 1457–1464. https://doi.org/10.1021/ja01863a037.

(63) Reddy, U. V.; Bowers, M.; Loganathan, N.; Bowden, M.; Yazaydin, A. O.; Kirkpatrick, R. J. Water Structure and Dynamics in Smectites: X - Ray Di Ff Raction and 2 H NMR Spectroscopy of Mg − , Ca − , Sr − , Na − , Cs − , and Pb − Hectorite. **2016**. https://doi.org/10.1021/acs.jpcc.6b03431.

(64) Yeh, J. J.; Lindau, I. Atomic Subshell Photoionization Cross Sections and Asymmetry Parameters: 1 - Z - 103. *At. Data Nucl. Data Tables* **1985**, *32* (1).

(65) Kjellander, R.; Marčelja, S.; Quirk, J. . Attractive Double-Layer Interactions between Calcium Clay Particles. *J. Colloid Interface Sci.* **1988**, *126* (1), 194–211. https://doi.org/10.1016/0021-9797(88)90113-0.

TOC Graphic